Optical fibre nanotips fabricated by a dynamic chemical etching for sensing applications

A. Barucci,[1,a)] F. Cosi,[1] A. Giannetti, [1]S. Pelli, [1]D. Griffini, [4] M. Insinna, [4] S. Salvadori, [4] B. Tiribilli, [3] and G.C. Righini[1,2]

[1] *IFAC-CNR, Nello Carrara Institute of Applied Physics, Via Madonna del Piano 10, Sesto Fiorentino 50019, Italy*

[2] *Enrico Fermi Centre, Piazza del Viminale 1, Roma 00184, Italy*

[3] *ISC-CNR, Institute for Complex Sistems, Via Madonna del Piano 10, Sesto Fiorentino 50019, Italy*

[4] *DIEF, Department of Industrial Engineering, University of Florence, via di S. Marta 3, Firenze 50139, Italy*

Nanoprobe tips are key components in many applications such as scanning probe microscopes, nanoscale imaging, nanofabrication and sensing.
This paper describes a dynamic chemical etching method for the fabrication of optical nanoprobes. The tips are produced by mechanically rotating and dipping a silica optical fibre in a chemical etching solution (aqueous hydrofluoric acid) covered with a protection layer.
Using different dynamic regimes of the mechanical movements during the chemical etching process it is possible to vary the cone angle, the shape and the roughness of the nanoprobes. It is found that the tip profiles are determined by the nonlinear dynamic evolution of the meniscus of the etchant near the fibre.
Computational fluid dynamic (CFD) simulations have been performed, showing that different flow regimes correspond to different shear forces acting on the forming nanotip, in agreement with experimental results.
With this method a high yield of reproducible nanotips can be obtained, thus overcoming the drawbacks of conventional etching techniques.
Typical tip features are short taper length (~200 μm), large cone angle (up to 40°), and small probe tip dimension (less than 30 nm).

I. INTRODUCTION

Fibre-optic nanoprobes have opened up new applications ranging from scanning probe microscopes, nanoscale imaging, and nanofabrication to molecular biology and medical diagnostics[1]. Due to their small sizes, this type of nanosensor provides important tools for minimal invasive analysis. Since transmission efficiency and detection sensitivity are highly related to the aperture size, the control of the nanoaperture shape and dimension is essential for the fabrication of high-quality nanoprobes.
Optical fibre nanotips can be produced traditionally by several methods[2], e.g. by the heating and pulling method[2, 3] or by chemical etching[4-12] and their variations, always achieving apex diameters smaller than 50 nm. Desirable properties of such probes are high brightness, obtained by large cone angles, a well defined circular aperture, no light leaking through pinholes in the metal coating, and a high optical damage threshold.[13-16]
In the heating and pulling method the optical fibre is heated by a CO_2 laser or a filament, then it is pulled apart with controlled force and speed, producing long tips.

This technique requires expensive equipment and complicated manipulations to precisely control tip diameter and transmission efficiency.

Conversely, chemical etching is a low cost and convenient method to fabricate nanotips, allowing the production of fibre tips with a higher optical throughput thanks to the possibility of fabricating shorter cones and larger cone angles in comparison to heating and pulling methods. The method is based on etching glass fibres at the meniscus between hydrofluoric acid and an organic overlayer (Turner method).[4, 17-26]

In this case, a tip is formed due to the decreasing meniscus dimension/width as the fibre is shortened by the etchant. Static etching, owing to its ease of operation, is widely employed.

Chemical etching process is usually well controlled by changing the etching solution, the overlayer liquid and/or etching time.

However, a well-known problem of etched tips is the sensitivity of the tip shape to environmental influences such as vibrations, temperature drifts, etc. during the etching process, resulting in low control of the process. Low control reflects on roughness and asymmetry of the tip apex, which are generally considered responsible for pinholes in the subsequently applied metal coating and ill-defined optical apertures, respectively.

Moreover, in most etching techniques, only the properties of the protecting layer determine the shape and contact angle of the meniscus. Therefore, the choice of the overlayer determines the cone angle.

All methods share the same goal of finding a way to precisely control aperture size, taper shape and roughness.

II. METHOD DESCRIPTION

In this paper, we describe and study a dynamic chemical etching method (patent pending), [27] aimed to overcome the main drawbacks of optical fibre chemical etching techniques.

Our method is based on a combination of mechanical movements, which, coupled to chemical etching, allows a better control of the shape and roughness of a fibre optical nanoprobe.

The stripped optical fibre end is dipped into a vial containing an aqueous hydrofluoric acid (HF) solution. The vial and the optical fibre are connected to motors allowing them to rotate independently around the fibre and the vial axis respectively. Moreover, the vial and the optical fibre are equipped with precision translation stages, for alignment of the fibre on the rotation axis of the vial.

A special vial has been designed and fabricated in order to preserve the precise alignment of the axis of rotation of optical fibre and the vial during the rotation and extraction of the fibre (Figure 1).

The basic idea of our method is to use rotation movements to generate different kind of flows inside the vial, which will be reflect in different kind of shapes and surface characteristics of the obtained nanoprobes, producing different transmission efficiency.[28-29-30]

III. RESULTS AND DISCUSSION

A. Experimental results

To demonstrate the flexibility of our method, Figure 2 shows some examples of nanotips. In particular, in the first row two examples of short taper nanotips obtained by slow rotation are shown (case a - b).

The taper length in these cases is about 200 μm. Instead, in c) - d) two examples of linear profile (c) obtained by slow rotation, and curved profile obtained by fast rotation (d), are shown. Four examples of fibre nanotips cone angles are shown in the second row, with a nanotip obtained by slow rotation resulting in a cone angle of about 40° (e), and a nanotip obtained by faster rotation resulting in a cone angle of about 25° (f). The case g) is an example of combined movements, rotation and extraction, resulting in a cone angle of about 7°, while case h) shows a cone angle of about 14° resulting from only extraction. Moreover, in the third row some examples of fibre nanotips apexes are shown, with dimension of the tip estimated about 30 - 40 nm in the case i) – l), and about 25 nm in m). Picture n) is obtained by processing m) in order to enhance contrast.

Different regimes can be generated by changing the ratio between the angular velocities and the ratio between the radii of optical fibre and vial, ranging from laminar flow to the onset of chaotic flow.

The type of flow of the viscous HF solution caused by the rotation of the vial and the optical fibre can be described in the framework of the Taylor-Couette flow (TCF) theory[31, 32].

Experimental evidences are supported by CFD analysis in order to evaluate stresses acting on the forming optical fibre nanoprobe caused by differences in terms of flow structures.

The rotation of the optical fibre and the vial in fact affects the shape of the meniscus separating the two immiscible fluid phases (HF and overlayer) [33] and modifies the wettability of the optical fibre surface, thus changing the shape of the nanotips and roughness.

At the same time, rotation modifies the time scale of the etching process and the diffusivity dynamics of the system.

Several different types of single-mode and multimode optical fibres were tested (e.g. Corning SMF-28, inner core diameter about 8 micron; 3M inner core diameter 3 micron; Nufern, inner core diameter 3 micron; 3M, inner core diameter 480 micron), all of them resulting in nanotips with similar features.

The effect of rotation on the nanotip shape can be seen in the Figure 3, where three representative cases are compared. A static etching and two dynamic cases (low and high rotation velocities) are considered. A representative AFM image (10 μm x 10 μm) is presented in Figure 3, one for each considered case. They evidence differences in the surface texture, for example larger ripples are present in case ‘b’ compared to case ‘c’. The averaged rms roughness decreases significantly for higher rotation speeds. The cone angle is changed too, ranging from 40° in case ‘a’ to 20° in case b and c. It’s worth to observe that the fibre diameter reduction due to the etching affects the peripheral velocities and then the shear forces on the surface.

Moreover, by an accurate control of the extraction speed of the fibre from the HF solution, we are able to control the length of the nanotip, and to minimize capillarity effects at the nanoscale, limiting strong friction on the optical fibre nanotip in the final part of the etching process[34, 35]. Obviously, the speed of extraction modifies the angle of the nanotip (Figure 2).

We would like to highlight that in spite of the significant torque exerted on the tip moving at that speed, especially if the fibre is slightly off center, in our experience more than 70% of the nanotips survive to the proposed fabrication process.

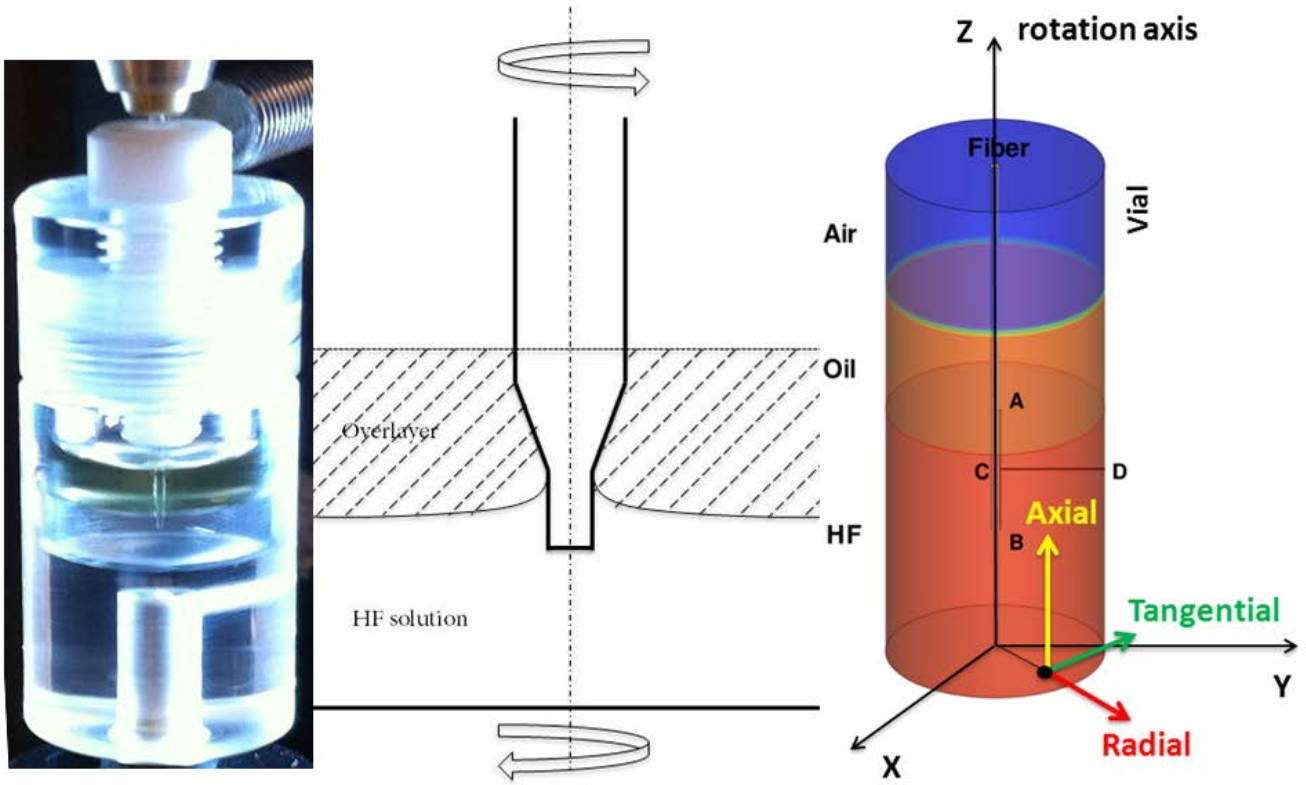

Figure 1: Optical fibre nanotip fabrication set-up. Left: picture of the system. The fibre is connected to a motor. The vial containing the HF acid solution and the oil is connected directly to the underlying motor. The fibre is guided inside the solution by a funnel made of Teflon. The funnel inside the vial is used to prevent precession of the fibre. The whole set-up was designed and built in order to align the axis of rotation of optical fibre and vial.
Middle: sketch of the set-up. Right: 3D model used on CFD simulations. AB and CD represent lines along and perpendicular to the fibre axis respectively.

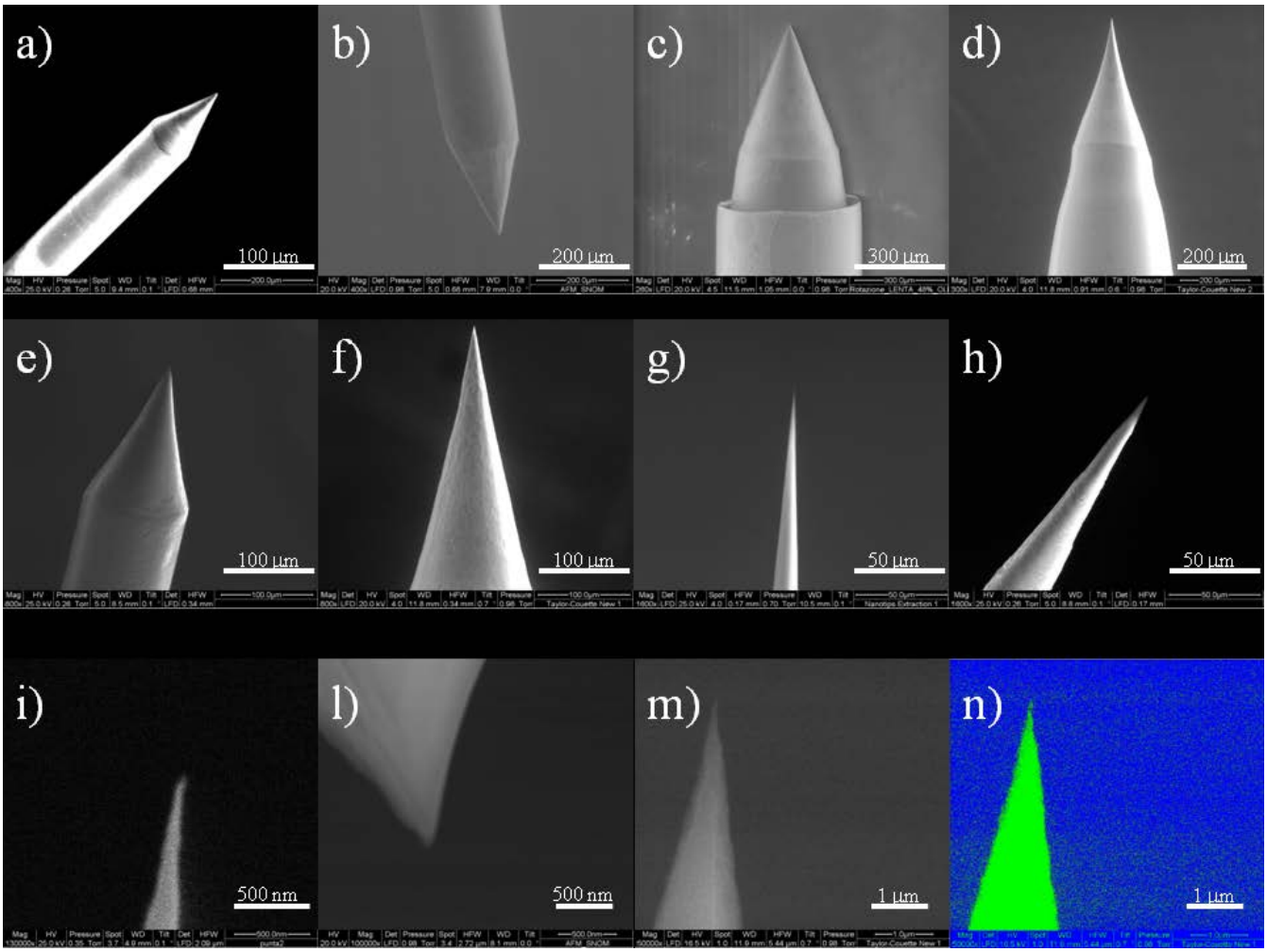

Figure 2: First line: a) - b) Examples of short taper nanotips obtained by slow rotation. A short taper length of about 200 micron has been obtained. First line: c) - d) Examples of profiles: c) linear profile obtained by slow rotation; d) curved profile obtained by fast rotation. Second line: examples of fibre nanotips cone angles. e) nanotip obtained by slow rotation resulting in a cone angle of about 40°; f) nanotip obtained by faster rotation resulting in a cone angle of about 25°; g) example of combined movements, rotation and extraction, resulting in a cone angle of about 7°; h) example of only extraction, resulting in a cone angle of about 14°. Third line: examples of fibre nanotips apex: i) - l) the dimension of the tip is estimated about 30 - 40 nm; m -n) nanometric tip estimated about 25 nm. Picture n) processed from m) in order to enhance contrast.

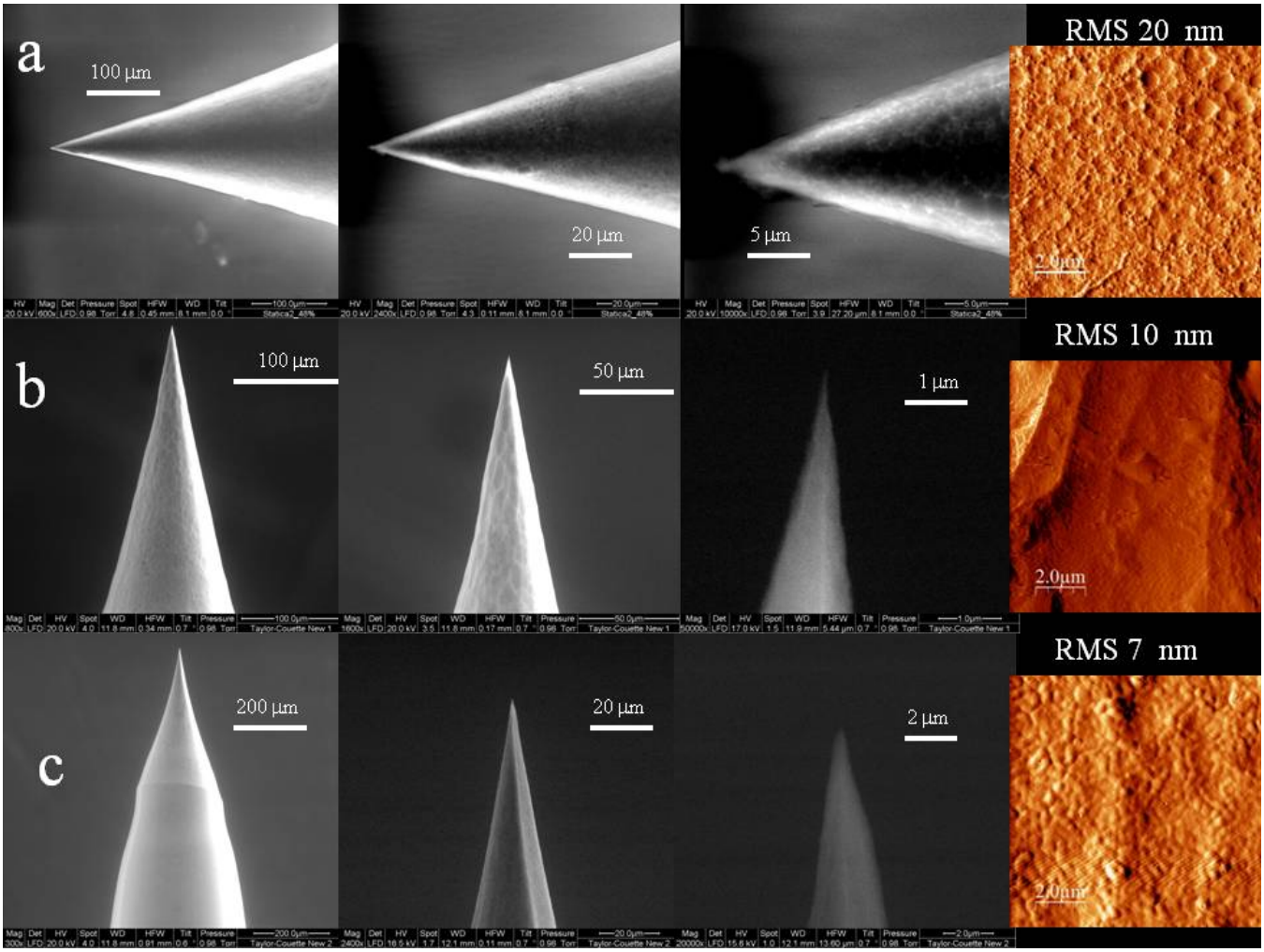

Figure 3: SEM images of optical fibre nanotips fabricated in 3 different ways. a) Static etching; b) Mixed method with vial turning at 3 rpm, fibre at 1000 rpm; c) Mixed method with vial turning speed at 17 rpm, fibre at 2000 rpm. Vial and optical fibre always rotates in opposite direction. HF 48%, vial with diameter 11.5 mm, Multimode 3M fibre with inner core of 480 µm. Overlayer of vegetal oil. On the right the AFM image of the surface are reported with the corresponding roughness measurements. Z range: a) 1.8 µm, b) 0.47 µm, c) 0.16 µm.

B. Fluid dynamic simulations

Experimental results have been supported by computed fluid dynamic simulations, evaluating the fluid behaviour of the Taylor-Couette flows generated under different operative conditions.

The geometrical model consists in a 3D domain with closed rotating boundaries and has been used to reproduce the experimental apparatus (Figure 1). The radius and the height of the vial are respectively 5.75 mm and 28 mm respectively, while the radius and the height of the fibre are 240 µm and 21 mm respectively.

Half height of the vial is filled with HF (density = 970 kg/m^3 and dynamic viscosity = 0.00092 Pas) a quarter with silicone oil (density = 950 kg/m^3 and dynamic viscosity = 0.019 Pas) and the remaining part with air at the atmospheric pressure and temperature (density = 1.225 kg/m^3 and dynamic viscosity = 1.7894 E-05 Pas). The fibre is immersed in the HF for 1/3 of its total height.

Fibre and vial are counter-rotating. Two representatives operative conditions have been analysed, a low rotational one (6.28 rad/s both for fibre and vial) referred as “Test Case Number 1” (TCN1) and a high rotational one (628 rad/s for the fibre and 18.85 rad/sec for the vial) referred as “Test Case Number 2” (TCN2).

Results, in terms of flow speed, are extracted along a radial section (line C-D), while shear stresses along the fibre are extracted along the line A-B (Figure 1).

Numerical simulations were carried out with the commercial code ANSYS Fluent ® on a structured grid. The code[36] is based on the Finite Volume Method and the pressure-based solver was chosen with a segregated algorithm (PISO) for the pressure speed coupling.

Time-resolved calculations are performed with a first order temporal discretization, using a second order upwind scheme for the spatial discretization and the Green-Gauss cell-based method for the gradients evaluation.

The Volume of Fluid model, specific for stratified/free-surface flows, was used with its explicit scheme.

Due to the remarkable difference in dynamical viscosity the Compressive Interface Capturing Scheme for Arbitrary Meshes (CICSAM) is used for the volume fraction interpolation.

Calculations are laminar due to the low Reynolds number of the flow and then no turbulent closure models have been used.

A forced steady state grid dependence analysis has been performed in order to evaluate the accuracy of the spatial discretization. The selected grid entails a difference of 0.7% in evaluating the fibre torque with respect to the finest one.

Three different levels of simulations were tested both for TCN1 and TCN2 with increasing numerical model accuracy. The base level does not account for Surface Tension and Wall Adhesion while the more accurate (referred as STWA) accounts for both.

The three models were compared in order to evaluate the differences obtained by the increasing accuracy level.

The comparison showed significant differences in terms of the interface surface shape and spurious currents sensitivity with a more physical interface reconstruction obtained by model STWA that resulted also to be the most sensible to spurious currents problem. However this numerical problem influences the flow field in confined regions without affecting the overall flow behaviour.

As a consequence, general results are not affected by the choice of the model showing same differences when comparing operative conditions.

Results are shown in terms of non-dimensional values. The reference values for velocities and stresses are respectively the tangential speed of the fibre and the averaged tangential stress obtained in the HF over the radius gap, both evaluated for TCN2.

Figure 4 (top) shows a vial-driven core flow directed upward at the vial wall and downward at the fibre wall both for the TCN1 and TCN2 operative conditions. The high-speed case however results in more complex flow structures with high intensity Taylor-Couette vortices generated in the influence area of the fibre. Configurations ranging from 3 to 7 vortices have been highlighted. Odd vortices are more stable while even ones have a shorter life due to their intrinsic instability.

Due to TCN2 unsteady behaviour when comparing the operative conditions, a TCN2 average value is plotted together with its maximums and minimums envelope curves.

The evaluation of the tangential speed field (shown in Figure 4a) shows the influence areas of the rotating vial and counter-rotating fibre. In fact negative non-dimensional tangential speed is induced by the rotation of the fibre while positive non-dimensional tangential speed is due to the rotation of the vial. It is evident that under TCN1 condition the area of influence of the fibre is almost negligible and hence the fluid is completely driven by the vial giving the rotating core flow previously described. On the contrary, TCN2 shows an area from 10% up to 33% of the gap between the fibre and the vial where the flow is driven by the high speed swirling fibre.

Coherently, axial speed (shown in Figure 4b), which accounts for vortices, concentrates the maximum variations in the first 20% of the gap where the flow is driven by the fibre. Non-dimensional axial speed peaks are 0.22 and -0.15 for the TCN2 while TCN1 values are 0.000125 at 55% of the gap and -0.0005 at 15% thus showing a difference of three orders of magnitude for the vortical flow field around the fibre.

Fibre stresses are also evaluated and compared. The non dimensional tangential shear stress at the interface zone (where the meniscus generating the nanoprobe is located) has a value of -0.7 for the TCN1, while TCN2 has an average value of -46 with a maximum of -175 and a minimum of -28 thus having two to three orders of magnitude difference between the two cases tangential stresses.

Figure 5 shows characteristic axial shear stresses on the fibre. Yet again orders of magnitude are completely different, with TCN1 having a -0.005 non-dimensional shear stress and TCN2 ranging from 21 to -23. The TCN2 average line shows a five vortices structure behaviour that in fact resulted as the more stable and frequent condition in the TCN2 chaotic motion.

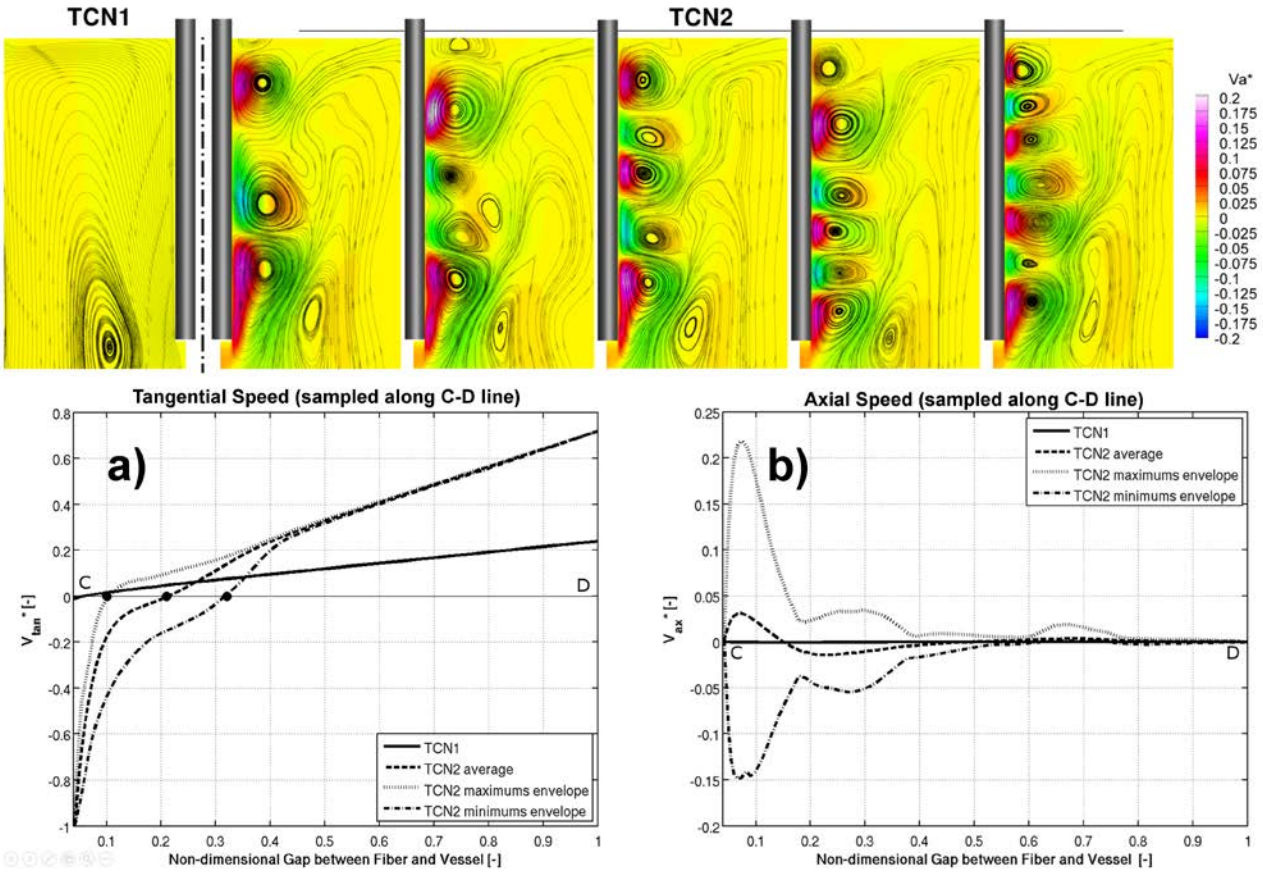

Figure 4: Comparison between TCN1 and TCN2 cases. Top: characteristic vortical structures in a plane containing the fibre rotation axis. Bottom: tangential (a)) and axial (b)) speed fields sampled along the C-D line (shown in Figure 1 right).

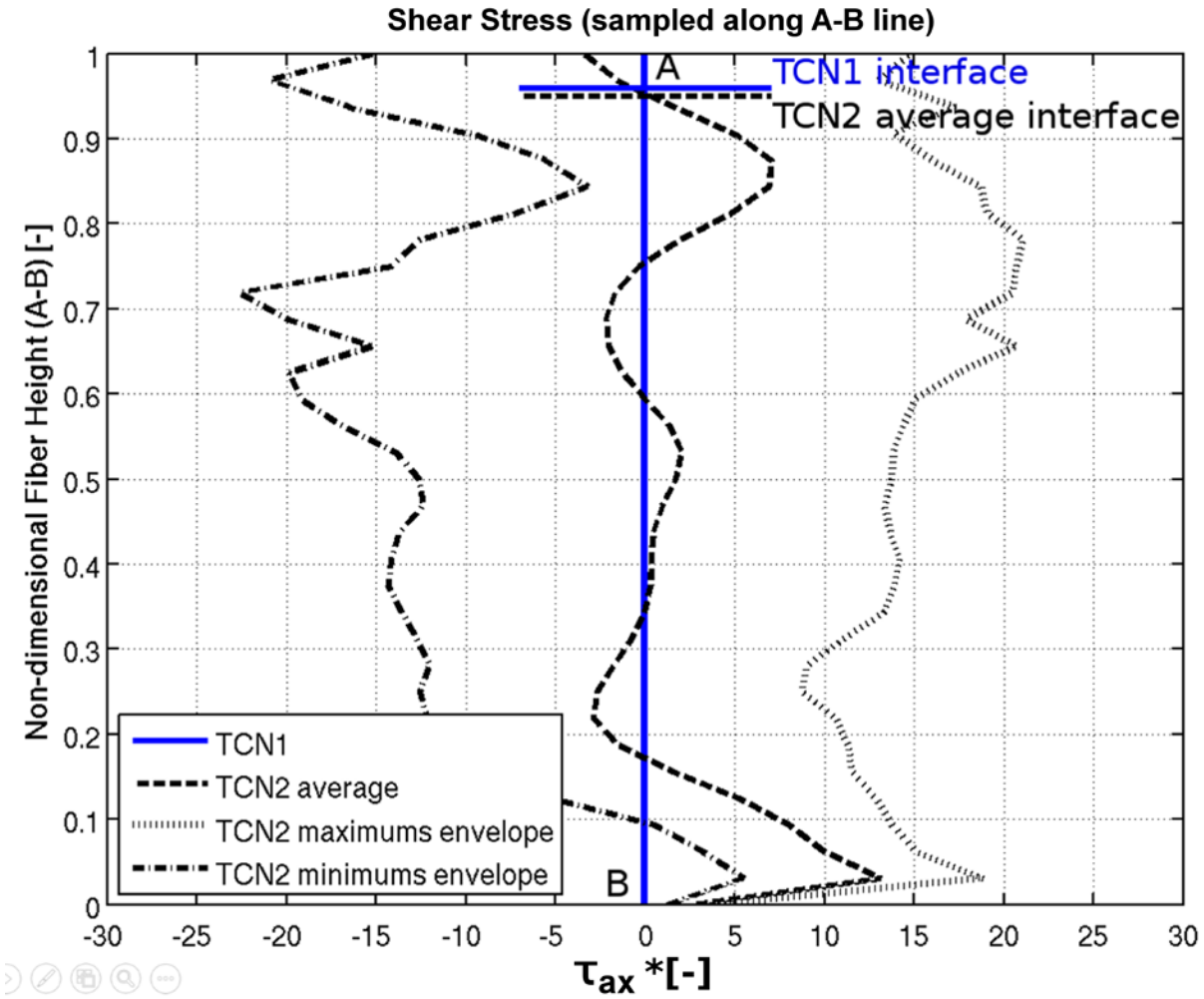

Figure 5: Axial shear stress sampled along A-B line (shown in Figure 1 right).

IV. CONCLUSIONS

In conclusion, in this paper we have investigated a new dynamic chemical etching, revealing the potential to fabricate optical fibre nanotips of particular shape, cone angle and roughness, properly varying the dynamic mechanical parameters. Some representative cases were considered and investigated.

Different rotation speeds correspond to different fluid dynamic regimes, as clearly evidenced by the CFD simulations, and allow the production of different kind of nanotips. In particular we found that higher velocities provide lower roughness of the surface.

With our method optical fibre nanoprobes with distal end smaller than 30 nm, cone angle ranging from 15° to 40° and roughness below 10 nm can be fabricated with high yield and reproducibility. The nanometric roughness is the key point to have an optimal metal coating deposition or a good chemical functionalization for sensing applications.

ACKNOWLEDGEMENTS

The authors wish to thank F. Baldini for fruitful discussions, R. Calzolai for technical assistance and project FIRB ITALNANONET for financial support.

References

1. Y. Zhang, A. Dhawan, T. Vo-Dinh, et al., Nanoscale Res Lett., **6**:18 (2011).
2. B. Hecht, et al., The Journal of Chemical Physics, **112**, 7761-7774 (2000).
3. G. A. Valaskovic et al., Appl. Opt., **34,** 1215 (1995).
4. D. R. Turner, U.S. patent 4469-554 (1983).
5. N. Gu, et al., J. Vac. Sci. Technol. B, **22**, 2283 (2004).
6. R. Stockle, Appl. Phys. Lett., **75**, 160 (1999).
7. A. Lazarev, et al., Rev. Sci. Instrum., **74**, 3679 (2003).
8. P. Hoffmann, et al., Ultramicroscopy, **61**, 165 (1995).
9. N. Essaidi, et al., Appl. Opt., **37**, 609 (1998).
10. T. Okayama, et al., Opt. Rev., **12**, 25 (2005).
11. M. Tao, et al., J. Opt., **12,** 015503 (2010).
12. Y. Yuan, et al, Appl. Opt. **51**, 5845 (2012).
13. D. W. Pohl, Adv. Opt. Electron Microsc., **12**, 243 (1991).
14. E. Betzig, et al., Appl. Phys. Lett., **60**, 2484 (1992).
15. L. Novotny, et al., Opt. Lett., **20**, 970 (1995).
16. J. A. Hoffmann, et al., Review of Scientific Instruments, **83**, 103703 (2012).
17. S. Monobe, and M. Ohtsu, J. Lightwave Technol, **14** (10), 2231-5 (1996).
18. D. Zeisel, et al., Appl. Phys. Lett., **68**, 2941 (1996).
19. B. A. F. Puygranier, et al., Ultramicroscopy, **85**, Issue 4, 235 (2000).
20. J. Yang, et al., Journal of Microscopy, **228**, 40 (2007).
21. A. Sayah, et al., Ultramicroscopy, **71**, Issues 1–4, 59 (1998).
22. S. Patanè, et al., Ultramicroscopy, **106**, Issue 6, 475 (2006).
23. P. K. Wei, et al., Journal of Microscopy, **210**, 334 (2003).
24. R. Stockle, et al., Appl. Phys. Lett., **75**, 160, (1999).
25. P. Lambelet, et al., Appl. Opt., **37**, 7289 (1998).
26. T. Okayama, et al., Optical Review, **12**, N. 1, 25 (2005).
27. A. Barucci, et al., Patent Pending PCT/EP2014/071743, filed on 10/10/2014.
28. B.I. Yakobson, and M.A. Paesler, Ultramicroscopy, **57**, 204 (1995).
29. A. LaRosa, B. I. Yakobson, and H.D. Hallen, APL **67** (18), 2597-2599 (1995).
30. W. Zhu, et al., Opt. Express, **21**, 28103 (2013).
31. G. I. Taylor, Philosophical Transactions of the Royal Society of London. Series A, Containing Papers of a Mathematical or Physical Character, **223**, 289 (1923).
32. C. D. Andereck, et al., Journal of Fluid Mechanics, **164**, 155 (1986).
33. M. P. Aronson, et al., J. Chem. Soc., Faraday Trans. 1, **74**, 555 (1978).

34. J. W. Van Honschoten, et al., Chem. Soc. Rev., **39**, 1096 (2010).
35. P. Prokopovich, et al., Advances in Colloid and Interface Science, **168**, Issues 1–2, 210 (2011).
36. ANSYS Inc., Fluent v14, Ansys Fluent Theory guide.